Integrated Aeroelastic and Control Analysis of Wind Turbine Blades Equipped with Microtabs

Terence Macquart and Alireza Maheri
Faculty of Engineering and Environment, Northumbria University, UK

Abstract

This paper presents the results of an investigation into the performance of different controllers in active load control of wind turbine blades equipped with microtabs. A bang-bang (BB) controller, a linear quadratic regulator (LQR) a proportional integral derivative (PID) and a sliding mode controller (SMC) are synthesised for load alleviation. The performance of the synthesised controllers in load alleviation is evaluated by employing WTAC (Wind Turbine Aeroelastic and Control), a wind turbine simulator incorporating an unsteady aerodynamic module, a structural analysis module and a control module. The variable-speed pitch-controlled NREL-5MW is adopted as the case study. Using frequency domain analysis it is shown that for the studied case all controllers have more or less the same performance at rejecting the first rotational frequency loads. It is also shown that all controllers are more effective at rejecting loads with lower frequencies. BB and PID controllers, although capable of rejecting low frequency loads, may cause amplification of loads with higher frequencies. Investigating the performance of four controllers at different wind speeds for the studied wind turbine, it is observed that the effectiveness of BB and PID controllers reduces with wind speed but on the other hand SMC and LQR perform better at higher wind speeds. Introducing a new parameter, life index, the performance of different controllers in terms of the actuation wear is investigated. It is shown that LQR cause less actuation wear compared to SMC, while having comparable performance in load alleviation.

Keywords: microtab; load alleviation; sliding mode control; linear quadratic control; bang-bang control; proportional integral derivative control; WTAC

1 Introduction

Wind turbines are subjected to cyclic and stochastic loads produced by wind shear, tower shadow, yaw misalignment, wind turbulence and, in case of operating in a wind farm, the wake effects of other turbines. The unsteady loads acting on rotor blades are spread out over a wide range of frequencies and affect the extracted wind energy by the rotor as well as the lifespan of the blades and other mechanical and structural components. The effect of the flow unsteadiness on the fatigue life of blades increases with the size of wind turbines. Individual pitch control systems are currently employed in many modern wind turbines as a means of alleviating loads. Although individual pitch control systems have shown great performance in cyclic load alleviations of 1*P* (rotor rotational frequency) [1] up to 3*P* [2], these systems do not have any significant impact on stochastic loads with higher frequencies. In contrast to individual pitch control systems, other active flow controllers use aerodynamic control surfaces such as trailing edge flaps and microtabs to modify the flow kinematics locally [3, 4]. Microtabs, proposed by Yen et al. in 2000 [5], are small tabs located near the aerofoil trailing edge. These tabs deploy almost normal to the surface of the blade on the pressure and suction sides. The deploying height is about 1% to 2% of the local chord length. In comparison to trailing edge flaps, which have been extensively studied for helicopter blades applications, load alleviation using microtabs is a relatively new field of research. Most of earlier research works on microtab were focused on its effectiveness in changing the aerodynamic performance of aerofoils [5-8]. These works, carrying out numerical and experimental analysis, investigate microtabs steady and transient aerodynamic response and the effect of microtab deployment height and location on the aerodynamic characteristics of the host aerofoils. More recently, applying those results, research on microtab has become more focused on its performance in wind turbine blade load alleviation [9-13]. The load alleviation results presented by Wilson et al. [10-11], although promising, were obtained via simulations based on a simplified aerodynamic model for microtabs. The microtab response and its effect on the flow kinematics were assumed to

be instantaneous, providing the same amount of lift and drag forces as the steady state data. In another research work by Zayas et al. [12] the transient response of microtab was included. However their conclusion is not supported by any quantitative results. More recently, in their studies Gaunaa et al. [9] and Macquart et al. [13] used a bang-bang (BB) controller with more realistic dynamic microtabs for predicting the blades aerodynamic performances.

The research presented in this paper, while a continuation of the previous research on microtabs, is more focused on the control aspect of microtabs. In this paper the wind turbine blade load alleviation is approached from a control perspective, investigating: (i) the design of more advance control strategy, (ii) the significance of measurement errors on active control, (iii) the microtabs actuation damage, and (iv) the load alleviation performances in the time and frequency domain. In this context, the steady state aerodynamic coefficients due to microtab deployment are obtained by carrying out two dimensional CFD analyses. Various microtab heights and locations are simulated to find those configurations which provide sufficient lift coefficient for active control with minimum penalty on drag. Furthermore, the microtab transient dynamic is modelled and coupled to a wind turbine blade finite element model. In comparison to the previous works, in this study the impact of flow measurement errors on the aerodynamic model predictions is also investigated. Moreover, the load alleviation performances of the microtab equipped blades are evaluated. For this purpose, two different microtab deployment mechanisms - continuous and discontinuous (on/off) - are considered and four controllers are proposed. The classical linear quadratic regulator (LQR) and proportional integral derivative (PID) controllers are suitable for continuous model whereas the BB and sliding mode controller (SMC) can be applied to both categories. The synthesised controllers are implemented in an unsteady blade element momentum theory (BEMT) based aerodynamic code coupled with a control and a structural module. In contrast to previous research works, the load alleviation obtained using microtabs are evaluated in both time and frequency domains.

Active flow controllers are required to meet design constraints in order to be considered as a viable solution for real applications. Microtabs are meant to reject unsteady loads due to wind turbulence and therefore have to withstand fast actuations to achieve their main objective. On the other hand, violent actuations may lead to damage and life reduction of the actuator. A trade-off strategy between those two objectives must be found such that loads are effectively alleviated while microtabs actuation does not significantly reduce the life of actuators leading to unwanted increase of the maintenance cost. The last part of this paper investigates the suitability of these controllers in terms of their actuations.

The rest of the paper is structured as follows. Section 2 elaborates on the dynamic modelling of microtab. Aero-structural modelling of blades equipped with microtabs is explained in Section 3, followed by explaining the four different controlling methods investigated in this paper in Section 4. Section 5 is dedicated to WTAC, the developed simulation and analysis tool and its performance evaluation against other similar software tools. Results of case studies for different controlling methods are presented and discussed in Section 6.

2 Microtab Aerodynamic Response Modelling

Previous studies [4, 5, 7, 13-15] have shown that microtab and gurney flap have similar behaviours and, for efficiency, that microtab should have a typical height of the order of the boundary-layer thickness of the aerofoil. More precise experiments and simulations, in particular for the S809 and DU-96-W-180 aerofoils demonstrated that microtab height above 2% of the chord length results in a significant increase in drag. Furthermore, computational investigations reported in [4] and [7] show that a 1% height microtab located at 95% of chord of the pressure side often provides a good lift/drag compromise. Effect of microtab on NACA 64-618, the aerofoil located at the outer part of the blade of NREL-5MW wind turbine [16], has not been previously investigated. This aerofoil,

compared to S809 is thinner and towards the trailing edge has a different curvature on the lower surface as shown in Figure 1. In this figure, the parameters c denotes the aerofoil chord length.

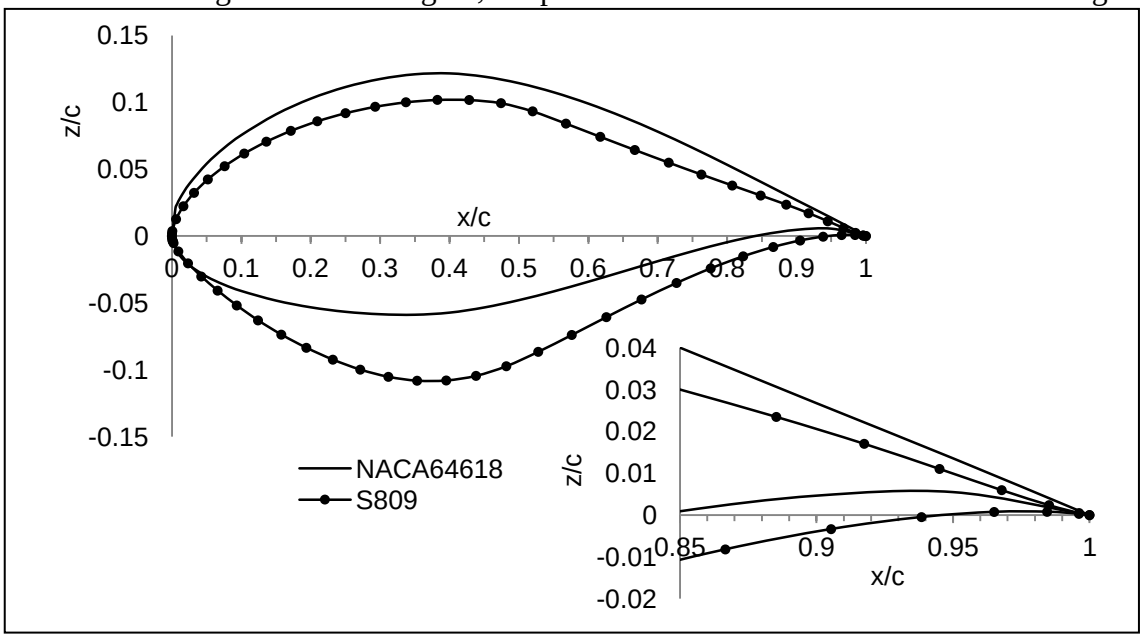

Figure 1 - S809 and NACA 64-618 profiles

Carrying out two-dimensional CFD analysis for several deployment heights and chord locations, it was found that on the lower surface, microtab located at 88% of chord from the leading edge with a deployment height of 2% of chord provide highest changes in lift coefficient with minimum penalty on drag coefficient. The best location and deployment height for the microtabs on the upper surface found as 91% and 1.1% of the chord length respectively. Figure 2 shows the effect of microtab deployment on the steady state lift and drag coefficients $\Delta C_{L,ss}$ and $\Delta C_{D,ss}$. In this figure, H_M and C_M, respectively, stand for the maximum microtab deployment height and microtab normalised location measured from the leading edge. Parameters H_M and C_M are both expressed in percentage of the chord length and *Lwr* and *Upr* refer the lower and upper surface of the aerofoil.

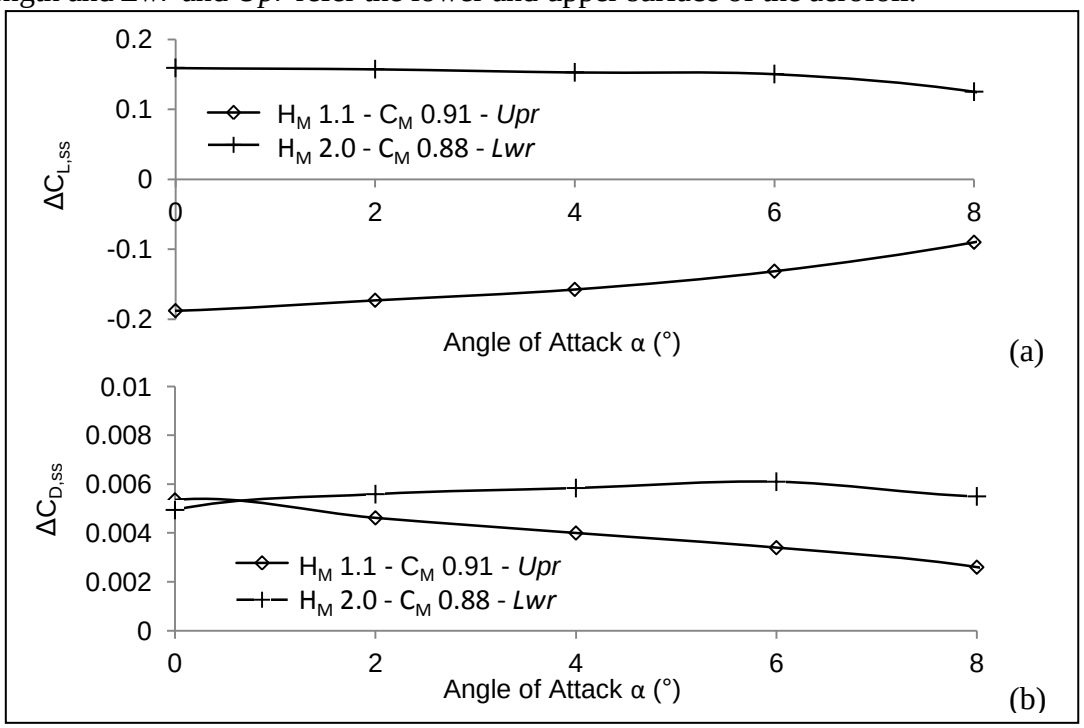

Figure 2 - Changes in (a) lift and (b) drag coefficients of NACA 64-618 aerofoil due to microtab deployment

The microtab dynamic response model recently developed by Macquart et al [13] is used for simulating the microtab transient aerodynamic response. This model is made up of a steady and a transient state, as shown in Figure 3.

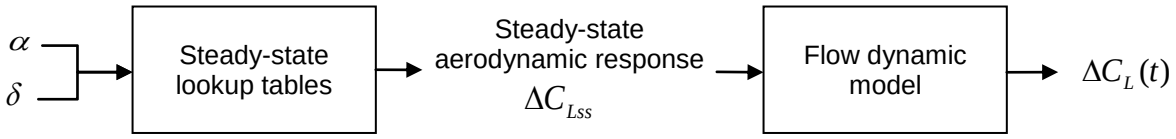

Figure 3 - Dynamic lift coefficient [13]

In this figure, parameter δ denotes the normalised microtab deployment height (deployment height divided by H_M), α is the local angle of attack, $\Delta C_{L,ss}$ is the steady state changes in the lift coefficient due to microtab deployment and ΔC_L is the dynamic (instantaneous) lift coefficient due to microtab deployment. The steady state data collected from two dimensional CFD analyses are used to generate the steady state lookup tables. For synthesising the controllers, the lookup tables are approximated by the surface of Equation 1 which is linear with respect to the microtab deployment height δ and nonlinear with respect to the aerofoil angle of attack α.

$$\Delta C_{L,ss}(\delta,\alpha) = K_1\delta \tag{1.a}$$

$$K_1 = a_1\alpha^5 + a_2\alpha^4 + a_3\alpha^3 + a_4\alpha^2 + a_5\alpha + a_6 \tag{1.b}$$

where, a_1 to a_6 are constants found to minimise the error in surface fitting.

The CFD steady state data and its linear approximation obtained by Equation 1 are plotted in Figure 4. As one can observe, the surface function is linear enough with respect to the microtab deployment height δ for the linear approximation to give accurate results.

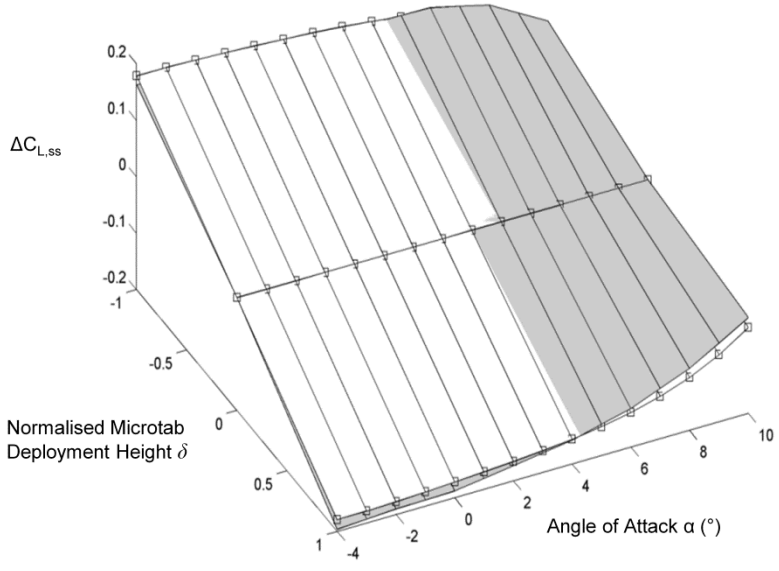

Figure 4 - Linear approximation of the effect of microtab on steady state lift coefficient for NACA 64-618 aerofoil ($rms = 0.01071$)

The flow dynamic model, in Figure 3, is described in the Laplace domain by Equation 2 [13].

$$\frac{\Delta C_L}{\Delta C_{Lss}} = \frac{0.5}{1+\tau_f s} + \frac{0.5}{1+\tau_s s} \tag{2}$$

where ΔC_L stands for the dynamic lift coefficient, and parameters τ_f and τ_s are the time constants representing the fast and slow dynamics respectively. More details on the subject can be found in references [6, 9, 13]. Combining the model of Equation 1 with the flow dynamic response of Equation 2, the overall microtab dynamic from deployment to impact on the lift coefficient can be obtained. Additionally, this microtab dynamic model takes into account two constraints: (i) the effect of microtab on the local lift coefficient is limited to the steady state value of ΔC_{Lss} at maximum tab deployment, and (ii) the time required for the full microtab deployment is fixed [6, 13]. Knowing the microtab deployment height, the deployment time is used to calculate the maximal deployment speed.

The model presented in Equation 2 is used to represent the microtab dynamic as shown for a typical microtab deployment and aerodynamic response as in Figure 5.

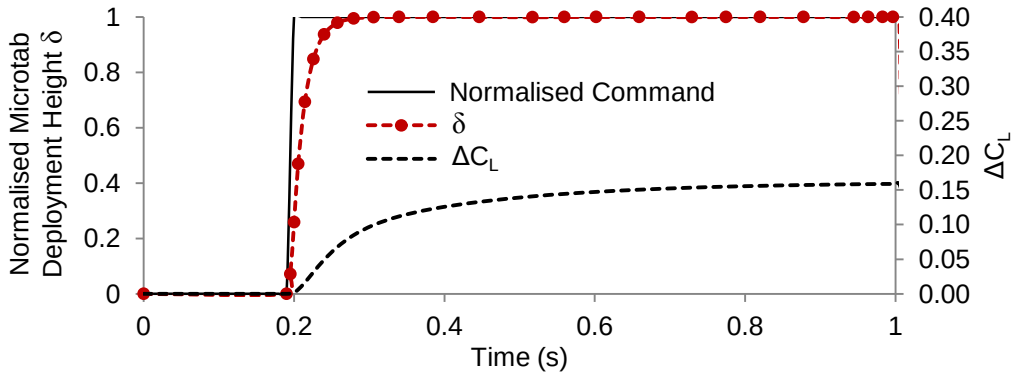

Figure 5 - Typical dynamic lift generated by microtab response to full deployment

3 Aero-Structural Modelling

Manipulating unsteady flow using active flow controllers is a multi-disciplinary science involving aerodynamics, structural dynamics and control, facing challenges due to large and complex non-linearities as well as couplings. One way to tackle this problem, referred to as reduced order model (ROM), is to use a simplified version of the system dynamics while conserving reasonable accuracy for calculations. Collis [17] advocates that ROMs are crucial in active flow control as real flow dynamics are usually highly non-linear and have high-dimensionality. In this context, a finite element (FE) code, using planar frame elements, has been developed to analyse the blade structural dynamics as a rotating tapered beam. A modal transformation is then used to reduce the model size by only keeping the natural frequencies that are necessary for accurate dynamic motions.

3.1 Blade Structure Modal Model

The general governing equation of motion for the blade structural dynamic is given as:

$$[M]\ddot{\vec{X}}_d + [D]\dot{\vec{X}}_d + [K]\vec{X}_d = \vec{F} \qquad (3)$$

where, $[M]$, $[D]$ and $[K]$ are, respectively, the mass, damping and stiffness matrices, $\vec{F}$ is the force vector and $\vec{X}_d$ is the state vector containing nodal displacements and rotations. The structural damping is assumed to be a linear combination of the mass and stiffness, as given in Equation 4.

$$[D] = a_d[M] + b_d[K] \qquad (4)$$

Coefficients a_d and b_d are chosen to set ξ_i, the damping ratio of the natural frequencies of the i-th mode ω_i, as in Equation 5. In this study, these coefficients are set such that the structural damping ratios of the first flapwise and edgewise modes match the NREL-5MW blades damping ratios.

$$\xi_i = \frac{\left(a_d + b_d \omega_i\right)^2}{2\omega_i} \tag{5}$$

Since matrices $[M]$, $[K]$ and $[D]$ are symmetric, the transformation matrix $[V_e]$, containing the orthogonal eigenvectors of the un-damped system ($D = 0$ in Equation 3), can be used to transform Equation 3 into the modal form of Equation 6.

$$[M_q]\ddot{\vec{Q}} + [D_q]\dot{\vec{Q}} + [K_q]\vec{Q} = \vec{F}_q \tag{6}$$

in which, the modal coordinate vector $\vec{Q}$ and external force $\vec{F}_q$ are defined as:

$$\vec{Q} = [V_e]^{-1}\vec{X}_d, \tag{7}$$

$$[\vec{F}_q] = [V_e]^T[\vec{F}] \tag{8}$$

and diagonal modal matrices $[M_q]$, $[K_q]$ and $[D_q]$ are given by:

$$[K_q] = [V_e]^T[K][V_e] \tag{9}$$

$$[M_q] = [V_e]^T[M][V_e] \tag{10}$$

$$[D_q] = [V_e]^T[D][V_e] \tag{11}$$

Matrices $[M_q]$, $[D_q]$, $[K_q]$ and $[V_e] \in \Re^{(N_e N_{DOF})\times(N_e N_{DOF})}$ and vectors $\vec{Q}$ and $\vec{F}_q \in \Re^{(N_e N_{DOF})\times 1}$, where, N_e and N_{DOF} denote the number of elements and the number of degree of freedom per node respectively. The generalised force vector $\vec{F}$ in Equation 8 is obtained through the transformation of the distributed external forces as:

$$[\vec{F}]_{(N_e N_{DOF})\times 1} = [T]_{(N_e N_{DOF})\times N_e}[\vec{F}_{ext}]_{(N_e)\times 1} \tag{12}$$

The transformation matrix T is related to the blade mode shapes and can be found in any finite element books including forced beam motion.

Regrouping all the transformation matrices of the force vector into B_q Equation 6 can be rewritten in state space form as:

$$\begin{bmatrix}\dot{Q}\\ \ddot{Q}\end{bmatrix}_{(2N_e N_{DOF})\times 1} = [A_q]_{(2N_e N_{DOF})\times(2N_e N_{DOF})}\begin{bmatrix}Q\\ \dot{Q}\end{bmatrix}_{(2N_e N_{DOF})\times 1} + [B_q]_{(2N_e N_{DOF})\times(N_e)}[\vec{F}_{ext}]_{(N_e)\times 1} \tag{13}$$

where,

$$B_q = \begin{bmatrix} [0]_{(N_e N_{DOF}) \times N_e} \\ [M_q]^{-1} [V_e]^T_{(N_e N_{DOF}) \times (N_e N_{DOF})} [T]_{(N_e N_{DOF}) \times N_e} \end{bmatrix} \quad (14)$$

and

$$A_q = \begin{bmatrix} [0]_{(N_e N_{DOF}) \times (N_e N_{DOF})} & [I]_{(N_e N_{DOF}) \times (N_e N_{DOF})} \\ -[M_q]^{-1}[K_q] & -[M_q]^{-1}[D_q] \end{bmatrix} \quad (15)$$

This transformation results in a series of independent dynamic equations (Equation 13) with complex conjugates solutions representing the damped natural frequency of the structure. Because the system is now represented by independent equations of natural frequencies, it becomes possible to neglect particular frequencies that are not significantly contributing to the blade dynamic motion. For instance, if the first N_f natural frequencies are considered sufficient for accurate calculations, the modal model is obtained by removing all the rows and columns not corresponding to those modes. The resulting reduced model is shown in Equation 16, in which the subscript r stands for reduced.

$$\begin{bmatrix} \dot{Q}_r \\ \ddot{Q}_r \end{bmatrix}_{(2N_f) \times 1} = [A_{q,r}]_{(2N_f) \times (2N_f)} \begin{bmatrix} Q_r \\ \dot{Q}_r \end{bmatrix}_{(2N_f) \times 1} + [B_{q,r}]_{(2N_f) \times (N_e)} [\vec{F}_{ext}]_{(N_e) \times 1} \quad (16)$$

3.2 Blade Aeroelastic Model

The reduced structural model is then combined with the microtab aerodynamic model. In unsteady blade element momentum theory, the blades are divided into segments on which the external forces are assumed to be uniformly distributed and time dependent. It is also assumed that the implementation of the microtabs does not change the structural properties. In order to obtain the aero-structural coupling the external forces are divided into the control forces $\vec{F}_c$, produced by deployment of control surfaces and other external forces $\vec{F}_o$:

$$[\vec{F}_{ext}]_{(N_e) \times 1} = [\vec{F}_o]_{(N_e) \times 1} + [\vec{F}_c]_{(N_e) \times 1} \quad (17)$$

Considering the drag produced by microtabs to be negligible compared to the generated lift, the control forces producing flapwise moments generated by a microtab with its centre at radial location r can be expressed as:

$$F_c = \Delta C_L \frac{1}{2} \rho V_{rel}^2(r) c(r) \cos \alpha(r) \quad (18)$$

where, V_{rel} is the local relative velocity at span location r and ρ is the air density. Moreover, the dynamic lift produced by microtab actuation as shown in Section 2 can also be written in a general state space form as in Equations 19 and 20.

$$\dot{X}_m = A_m X_m + B_m u \tag{19}$$

$$\Delta C_L = [C_m] X_m \tag{20}$$

If the number of blade segments equipped with microtabs is denoted as N_c, $X_m \in \Re^{3N_c \times 1}$, $A_m \in \Re^{3N_c \times 3N_c}$, $B_m \in \Re^{3N_c \times N_c}$, $u \in \Re^{N_c \times 1}$, $C_m \in \Re^{N_e \times 3N_c}$ and $\Delta C_L \in \Re^{N_e \times 1}$.

Substituting for ΔC_L in Equation 20, back into Equation 18 one obtains:

$$F_c = [C_m] X_m \frac{1}{2} \rho V_{rel}^2 c \cos\alpha \tag{21}$$

One can then couple both aerodynamic and structural models as follow:

$$\begin{bmatrix} \dot{Q} \\ \dot{Q} \\ \dot{X}_m \end{bmatrix}_{(2N_f+3N_c)\times 1} = [A]_{(2N_f+3N_c)\times(2N_f+3N_c)} \begin{bmatrix} Q \\ \dot{Q} \\ X_m \end{bmatrix}_{(2N_f+3N_c)\times 1} + [B]_{(2N_f+3N_c)\times(N_e)} \left[\vec{F}_{ext}\right]_{(N_e)\times 1} \tag{22}$$

where the control input matrix can be rewritten as:

$$[B]_{(2N_f+3N_c)\times(N_e)} \left[\vec{F}_{ext}\right]_{(N_e)\times 1} = \begin{bmatrix} [B_{q,r}]_{(2N_f)\times(N_e)} \\ [0]_{(3N_c)\times(N_e)} \end{bmatrix} \left(\left[\vec{F}_o\right]_{(N_e)\times 1} + \left[\vec{F}_c\right]_{(N_e)\times 1} \right) = \begin{bmatrix} [0]_{(N_f)\times(N_e)} \\ [B_{q,r1}]_{(N_f)\times(N_e)} \\ [0]_{(3N_c)\times(N_e)} \end{bmatrix} \left(\left[\vec{F}_o\right]_{(N_e)\times 1} + \left[\vec{F}_c\right]_{(N_e)\times 1} \right) \tag{23}$$

Substituting $\vec{F}_c$ from Equation 21 into Equation 23 and re-arranging, the aero-structural model for multiple microtabs can be written in the state space form $\dot{X} = AX + Bu + D$ as in Equations 24.

$$\begin{bmatrix} \dot{Q} \\ \ddot{Q} \\ \dot{X}_m \end{bmatrix}_{(2N_f+3N_c)\times 1} = \begin{bmatrix} 0 & I & 0 \\ z_s & s_s & B_{q,r1} C_m Z \\ 0 & 0 & A_m \end{bmatrix}_{(2N_f+3N_c)\times(2N_f+3N_c)} \begin{bmatrix} Q \\ \dot{Q} \\ X_m \end{bmatrix}_{(2N_f+3N_c)\times 1} + \begin{bmatrix} [0]_{N_f \times Nc} \\ [0]_{N_f \times Nc} \\ [B_m]_{3Nc \times Nc} \end{bmatrix} \vec{u}_{(N_c \times 1)} + \begin{bmatrix} [0]_{N_f \times Ne} \\ [B_{q,r1}]_{N_f \times Ne} \\ [0]_{3N_c \times Ne} \end{bmatrix} \left[\vec{F}_o\right]_{Ne \times 1} \tag{24}$$

where

$$A = \begin{bmatrix} [0]_{N_f \times N_f} & [I]_{N_f \times N_f} & [0]_{N_f \times 3N_c} \\ [z_s]_{N_f \times N_f} & [s_s]_{N_f \times N_f} & [B_{q,r1} C_m Z]_{N_f \times 3N_c} \\ [0]_{3Nc \times N_f} & [0]_{3Nc \times N_f} & [A_m]_{3N_c \times 3N_c} \end{bmatrix} = \begin{bmatrix} [A_S]_{2N_f \times 2N_f} & [A_{AS}]_{2N_f \times 3N_c} \\ [0]_{3N_c \times 2N_f} & [A_m]_{3N_c \times 3N_c} \end{bmatrix} \tag{25}$$

and

$$Z = \frac{1}{2} \rho V_{rel}^2 c \cos\alpha \tag{26}$$

In Equations 25, the sub-matrix A_m corresponds to the aerodynamic model of the microtab, A_S corresponds to the structural model ($A_S = A_{q,r}$ in Equation 16), and A_{AS} represents the aero-structural coupling terms. The final system described in Equation 24 is naturally stable around the equilibrium point corresponding to zero blade displacement and zero microtab deployment.

As an example of a blade equipped with microtabs on one segment of the blade ($N_c = 1$) and keeping the three first natural frequencies ($N_f = 3$), the terms of the general state space form can be expanded as given in Equations 27 through 31.

$$\dot{X} = AX + Bu + D \tag{27}$$

$$X = \begin{bmatrix} Q_3 & Q_2 & Q_1 & \dot{Q}_3 & \dot{Q}_2 & \dot{Q}_1 & \delta & \Delta C_L & \Delta \dot{C}_L - r_1 \Delta C_{L,ss} \end{bmatrix}^T \tag{28}$$

$$A = \begin{bmatrix} [A_S]_{6\times6} & [A_{AS}]_{6\times3} \\ [0]_{3\times6} & [A_m]_{3\times3} \end{bmatrix} = \begin{bmatrix} \begin{bmatrix} 0 & 0 & 0 & 1 & 0 & 0 \\ 0 & 0 & 0 & 0 & 1 & 0 \\ 0 & 0 & 0 & 0 & 0 & 1 \\ z_3 & 0 & 0 & s_3 & 0 & 0 \\ 0 & z_2 & 0 & 0 & s_2 & 0 \\ 0 & 0 & z_1 & 0 & 0 & s_1 \end{bmatrix} & \begin{bmatrix} 0 & 0 & 0 \\ 0 & 0 & 0 \\ 0 & 0 & 0 \\ 0 & t_3 & 0 \\ 0 & t_2 & 0 \\ 0 & t_1 & 0 \end{bmatrix} \\ [0]_{3\times6} & \begin{bmatrix} e_1 & 0 & 0 \\ e_2 & 0 & 1 \\ e_3 & e_4 & e_5 \end{bmatrix} \end{bmatrix} \tag{29}$$

$$B = \begin{bmatrix} [0]_{N_f \times Nc} \\ [0]_{N_f \times Nc} \\ [B_m]_{3N_c \times Nc} \end{bmatrix} = \begin{bmatrix} 0 & 0 & 0 & 0 & 0 & 0 & 1 & 0 & 0 \end{bmatrix}^T \tag{30}$$

$$D = \begin{bmatrix} [0]_{N_f \times Ne} \\ [B_{q,r1}]_{N_f \times Ne} \\ [0]_{3N_c \times Ne} \end{bmatrix} [\vec{F}_o]_{Ne\times1} = \begin{bmatrix} 0 & 0 & 0 & F_{g1} & F_{g2} & F_{g3} & 0 & 0 & 0 \end{bmatrix}^T \tag{31}$$

In Equation 28, Q_is are the modal coordinates representing the first three natural frequencies of the blade. The last three terms of $\vec{X}$ correspond to the microtab response model. More details and the definitions of terms r_1 and $\Delta C_{L,ss}$ can be found in [13]. In Equation 29, the accuracy of z_i and s_i entries (i=1, 2, 3) directly depends on the number of elements in the finite element model of the blade. Parameters, t_i (i=1, 2, 3)and e_i (i=1, 2, 3, 4, 5), on the other hand depend on the lift generated by microtabs, the microtabs span location, their position with respect to the aerofoil leading edge, their maximum deployment height and deployment speed. In Equation 31, D stands for the state disturbance term (not to be confused with damping matrix in Equation 3).

Having determined the state vector $\vec{X}$, the system output $\vec{Y}$ can be determined:

$$\vec{Y} = C\vec{X} \tag{32}$$

in which, C is the blade deflection and estimated lift output matrix:

$$C = \begin{bmatrix} c_3 & c_2 & c_1 & 0 & 0 & 0 & 0 & 0 & 0 \\ 0 & 0 & 0 & 0 & 0 & 0 & 0 & 1 & 0 \end{bmatrix} \tag{33}$$

The entries of the first row of C relate the modal coordinates to the blade displacements or moments at a given location and the second row ensures availability of the generated lift. The entries of the C matrix depend on the available measurements (predicted inputs) and position of the sensors located along the blade span.

As one can see in Equation 29, the microtab dynamic is independent of the structural model. On the other hand, the three first blade natural frequencies depend on the dynamic force generated by the microtab deployment. It is, therefore, crucial to ensure that when aiming at alleviating loads of a particular frequency bandwidth or mode, the other modes are not exited.

4 Controller Design

In this section, the four controllers used for microtabs actuations are synthesised. The controllers are divided into the continuous and discontinuous types referring to the two microtab deployment mechanisms. The classical controllers such as PID and LQR are not suitable for discontinuous control command, whereas the BB and SMC can be used for both mechanism types. Although never more than one controller is used at the same time, one can represent the four controllers closed loop in one scheme as illustrated in Figure 6. In this figure, parameters Y , $\hat{Y}$, $\hat{Y}_{filt}$ and Y_r respectively denotes the system output (e.g. blade deflection or bending moment), estimated output, filtered output, reference for SMC. Moreover, parameter u represents the control command and $\hat{x}$ the state space estimated. The real time high-pass filter is designed to remove the low frequency content of the estimated system output $\hat{Y}$ caused by slow changes in incoming wind speeds. More precisely, because the lowest frequency to be alleviated correspond to the first rotational frequency, the filter attenuates all frequencies lower than 1P. The $\hat{Y}_{filt}$ signal therefore contains the entire bandwidth (1P+) of frequency to be alleviated. In other words, $\hat{Y}_{filt}$ is the closed loop error for the classical PID controller. Although it is quite common to use a band-pass filter for load alleviation, a simple high pass filter introduces fewer phase in the filtered signal. Furthermore, because the power spectrum of the measured signal decreases as the frequency increase, the controller naturally directs more control effort into the lower frequency content of the input signal.

Although the system output is locally measured (predicted output), it always contains noises. In order to remove measurements noises of the system output and to obtain the state vector required for implementing state controllers, the well-known Kalman filter is used. The construction of the Kalman filter is not detailed herein as this is a well-established procedure. Moreover, there are no major difficulties as the structural system is fully controllable and observable. On the other hand, the aerodynamic system is only partially observable since no sensor directly measures ΔC_L. The non-observed aerodynamic lift coefficient produce by microtabs is therefore directly calculated based on the flow measurements and dynamic model (Equation 19 and 20). More details about the controller design and the closed loop structure illustrated in Figure 6 are given through the rest of this section.

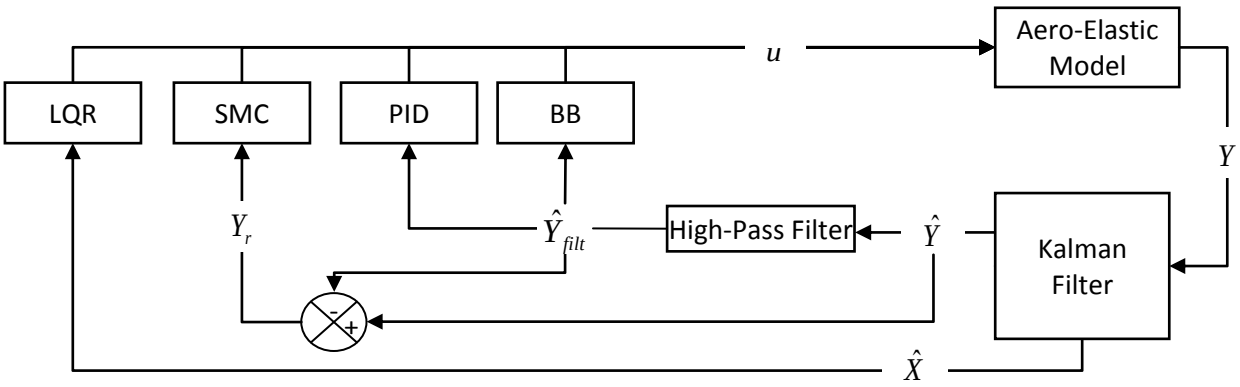

Figure 6 - Blade load alleviation closed loop control schematic of the four controllers.

4.1 Discontinuous Controllers

4.1.1 Bang-Bang Control

BB controllers are used in a large range of applications, such as hysteresis or discontinuous systems and space applications, particularly, where the systems are constrained to work in either on or off position. In order to keep microtab simple for implementations while featuring fast actuation response, robustness and low cost, Van Dam *et al* [8] proposed an on/off (BB) actuation mechanism. In comparison to more advanced controllers, BB controller does not require tuning, making it easier to implement.

The control law designed for BB controllers without hysteresis take the form of Equation 34.

$$u(t) = sign(\hat{Y}_{filt})U_{sat} \tag{34}$$

in which, U_{sat} stands for the maximum control value corresponding to the maximum microtab deployment height. Additionally, a small hysteresis is added to the control law for reducing potential over-actuation, see Figure 7. The BB control law employed in this study covers three cases: $u = 0$ for zero microtab deployment ($\delta_j = 0$) and $u = \pm U_{sat,j}$ corresponding to maximum deployment on the upper and lower surfaces ($\delta_j = \pm 1$).

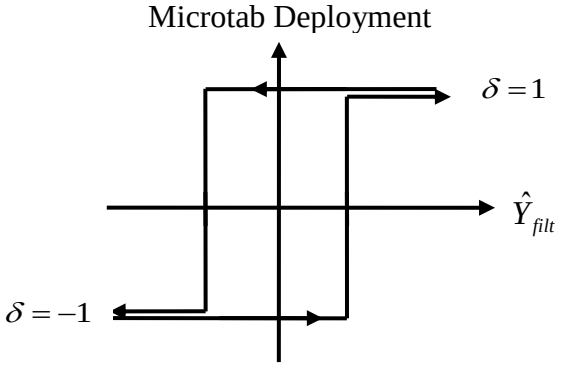

Figure 7 - BB controller with hysteresis

4.1.2 Sliding Mode Control

As for BB, the SMC has been chosen because its discontinuous nature makes it a suitable control method for on-off microtab actuators. In addition, the SMC can handle non-linearities and has advantageous features such as a low sensitivity to plant parameter uncertainties and noises. However, the control discontinuity causes chattering phenomenon that is one of the main drawback

of SMC controllers. The sliding surface is described by a 2nd order system dynamic of the system estimated output given by Equation 35:

$$S_1(x) = \ddot{Y} + \gamma\dot{Y} + \beta Y - \beta Y_r \tag{35}$$

with the condition of reaching the sliding surface in finite time:

$$S_1\dot{S}_1 \le -\kappa|S_1| \ , \ \kappa > 0 \tag{36}$$

Parameters γ and β are the coefficients describing the desired output dynamic and Y_r is the reference to track. As shown in Figure 6, $Y_r = \hat{Y} - \hat{Y}_{filt}$, indicating that the reference signal mostly contains the low frequencies of the estimated system output. By tracking Y_r the controller activates microtabs to reduce 1*P* and higher frequency loads.

The control ensuring that the condition given by Equation 36 is satisfied is denoted by u_d. Driving the surface derivative $\dot{S}_1$, the equivalent control law u_e is calculated by setting $\dot{S}_1 = 0$. The final control law is the summation of both controls as given by Equation 37.

$$u(t) = u_e(t) + u_d(t) \tag{37}$$

4.2 Continuous Controllers

Implementing continuous actuators for controlling microtabs deployment is more difficult and expensive than discontinuous actuators. However, this type of actuations gives the possibility to deploy microtabs at any given height lower than maximal, potentially increasing the performances of microtabs for active load control. In this study, both PID and LQR controllers assume the possibility of continuous microtab deployment for comparison with the discontinuous controller performances.

4.2.1 Proportional Integral Derivative Control

PID controllers are widely used in a variety of applications. The control law for PID controllers is given by Equation 38.

$$u(t) = K_P\varepsilon + K_D\varepsilon_D + K_I\varepsilon_I \tag{38}$$

in which, parameters K_I, K_D and K_P are respectively the integral, derivative and proportional tuning parameters. As in case of BB controller, the error signal $(\varepsilon = \hat{Y}_{filt})$ is obtained by filtering the system output to remove frequencies lower than the first rotational frequency. The frequency to reject therefore includes all frequencies higher or equal to 1*P*.

4.2.2 Linear Quadratic Regulator

LQR is widely used for linear systems. Tuning process for these controllers, compared to PID, is simple and straightforward. The blade load alleviation is ensured by using a state space augmented with the high-pass filter. The LQR control law is calculated in order to minimise a linear quadratic criterion of the form of Equation 39

$$J = \int_{t_0}^{t_f} \left(X^T Q_{lqr} X + u^T R_{lqr} u \right) dt \tag{39}$$

in which, the entries of Q_{lqr} and R_{lqr} matrices are weights. Solving the Riccati's equation for $S_{lqr}(t)$, the linear state feedback control law will be obtained as given by Equation 40.

$$u(t) = -R_{lqr}^{-1} B^T S_{lqr}(t) \vec{X}(t) \quad (40)$$

5 WTAC Performance

WTAC, the developed software tool for Wind Turbine Aeroelastic and Control analysis, consists of three modules, a blade aerodynamic code incorporating the microtab aerodynamic model of Section 2, the coupled structural model explained in Section 3, and the controllers synthesised based on the theory of Section 4. The blade aerodynamic module is a modified version of WTAero [18], which uses frozen wake for unsteady flow simulation incorporating Larsen's dynamic stall model [19]. Unsteady wind fields (with various mean wind speeds and turbulence types) are generated by TurbSim [20] in Cartesian coordinates. After adding the effect of wind shear, the resultant wind field is transformed to polar coordinates (r, θ) as required for the BEMT-based aerodynamic analyser WTAero. The control and aerodynamic modules use the blade deflection calculated using the structural module at the previous time step. A general overview of the structure of WTAC is presented in the flowchart of Figure 8 and pseudo code of the controller module is given in Fig. 9.

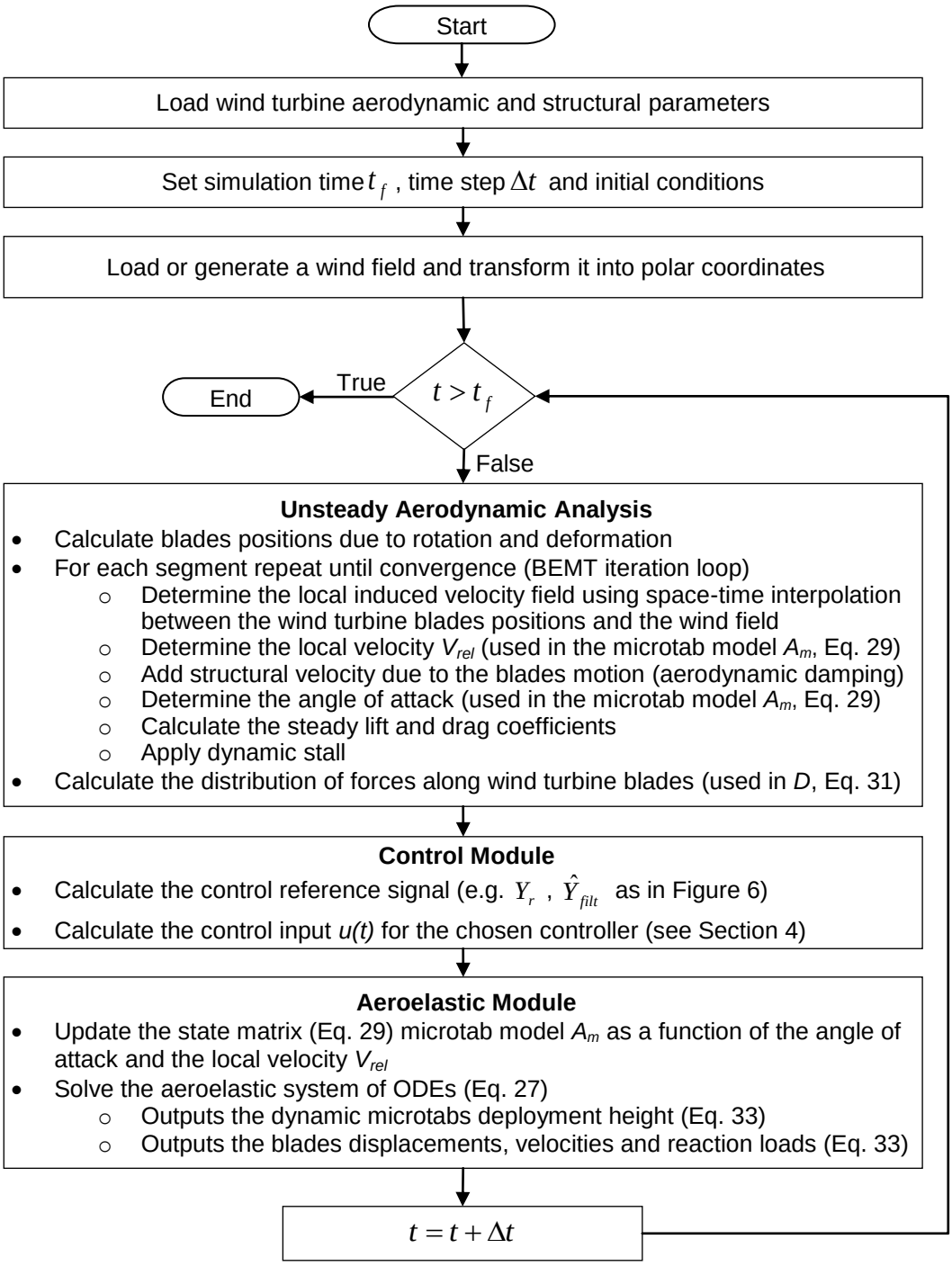

Figure 8 - Flowchart of wind turbine simulator WTAC

Control Module

- $Y(t)$ ← Measured system output (e.g. blade displacement or bending moment)
- Estimation of the blades state vector $\hat{X}(t)$ and displacement $\hat{Y}_i(t)$ using the Kalman filter
- If BB or PID control
  - Use the high-pass filter to remove the signal low frequencies $\hat{Y}_{filt,i}(t) \leftarrow filt\left(\hat{Y}_i(t)\right)$
  - If BB control calculate $U_i(t) = U_{i,\max}\left[sign\left(\hat{Y}_{filt,i}(t)\right)\right]_{hysteresis}$ (Eq. 34), End
  - If PID control calculate
    - The error $\varepsilon_i = \hat{Y}_{filt,i}(t)$ derivative $\varepsilon_{D,i}$ and integral $\varepsilon_{I,i}$
    - $U_i(t) = K_P\varepsilon_i + K_D\varepsilon_{D,i} + K_I\varepsilon_{I,i}$ (Eq. 38)
  - End
- End
- If LQR calculate $U_i(t) = -R_{lqr}^{-1}B^T S_{lqr}(t)\hat{X}(t)$ (Eq. 40), End
- If SMC
  - Use the high-pass filter to remove the signal low frequencies $\hat{Y}_{filt,i}(t) \leftarrow filt\left(\hat{Y}_i(t)\right)$
  - Calculate the desired displacement $Y_{r,i}(t) = \hat{Y}_i(t) - \hat{Y}_{filt,i}(t)$
  - Calculate the control law $U_i(t)$ according to Equation (37)
- End
- If $U_i(t) > U_{\max}$, $U_i(t) = U_{\max}$, End
- If $U_i(t) < -U_{\max}$, $U_i(t) = -U_{\max}$, End

Figure 9 - Pseudo-code of the controller module of WTAC

The performance of the aerodynamic code and the accuracy of the microtab aerodynamic response model have been previously evaluated and reported in [18] and [13]. In order to evaluate the performance of the developed finite element structural analyser, the rotating tapered beam benchmark of [21] and [22] is adopted. Results are shown in Table 1. The data presented in this table show that the results for natural frequencies are reasonably accurate.

Table 1 - Natural Frequencies of a Rotating Tapered Beam

Normalised Rotational speed	1st mode		2nd mode		3rd mode	
	[21 & 22]	WTAC	[21 & 22]	WTAC	[21 & 22]	WTAC
0	3.824	3.827	18.317	18.345	47.265	47.343
4	5.879	5.862	20.685	20.674	49.646	49.685
8	9.554	9.516	26.544	26.449	56.160	56.100
12	13.471	13.415	34.088	33.903	65.524	65.332

The aeroelastic performance of WTAC is compared with that of two nonlinear aeroelastic codes FAST [23] and DU-SWAMP [24]. Both steady and unsteady cases are considered for investigation. The nonlinear codes FAST and DU-SWAMP do not have the capability of simulating wind turbine blades equipped with microtabs. Therefore, to be able to compare the results, the sub-matrices corresponding to the effect of microtab are not considered in the coupled aero-structural model of WTAC. General characteristics of NREL-5MW wind turbine are given in Tables 2. More details and all data required for structural modelling can be found in [24].

Table 2 - Wind Turbine General Features

Hub height	87.6m
Diameter	126 m
Blade length	61.5m
Blade mass	17,740kg
Number of blades	3
Rated speed	12.1rpm
Structural blade damping for the first three modes (in percent of the critical damping)	<3%

Results of comparison are shown in Table 3 and Figures 10 and 11. Table 3 shows that WTAC generates results with acceptable accuracy considering that WTAC employs a linear structural model.

With reference to Figure 10, showing the steady state results, it can be seen that the predicted results by WTAC in some cases are closer to the predicted results by DU-SWAMP (e.g. rotor thrust force), while in some other cases WTAC results are closer to the results produced by FAST (the second part of the flapwise tip deflection curve and the first part of the power coefficient curve). In Figure 10, the discrepancies between the flapwise displacements of WTAC, DU_SWAMP and FAST are likely caused by a combination of factors. In DU_SWAMP the tower top deflection is included in the blade tip displacement [24]. WTAC does not include the flapwise and edgewise coupling. The three codes utilise different structural model (i.e. Super-Element, Finite Element, Multi-Body). Furthermore, non-linear structural phenomena are not considered in WTAC. On the other hand, in WTAC, the BEMT aerodynamic code employs a convergence accelerator algorithm ensuring convergence in its iteration loop at higher wind speeds [25].

Figure 11 shows the flapwise and edgewise tip displacements and the bending moments at the root of the blade at 15m/s mean wind speed, considering wind shear. This figure reveals similar dynamic behaviours whereas the flapwise offset is explained by the steady state discrepancies between FAST and WTAC. In addition, one can notice a slight phase shift between both predictions that can be attributed to different initialisation step.

Table 3 - Wind Turbine Blade Natural Frequencies

Blade natural frequencies(Hz)	FAST [23]	WTAC
1st Flapwise	0.6993	0.6881
2nd Flapwise	2.0205	1.9895
1st Edgewise	1.0793	1.0852

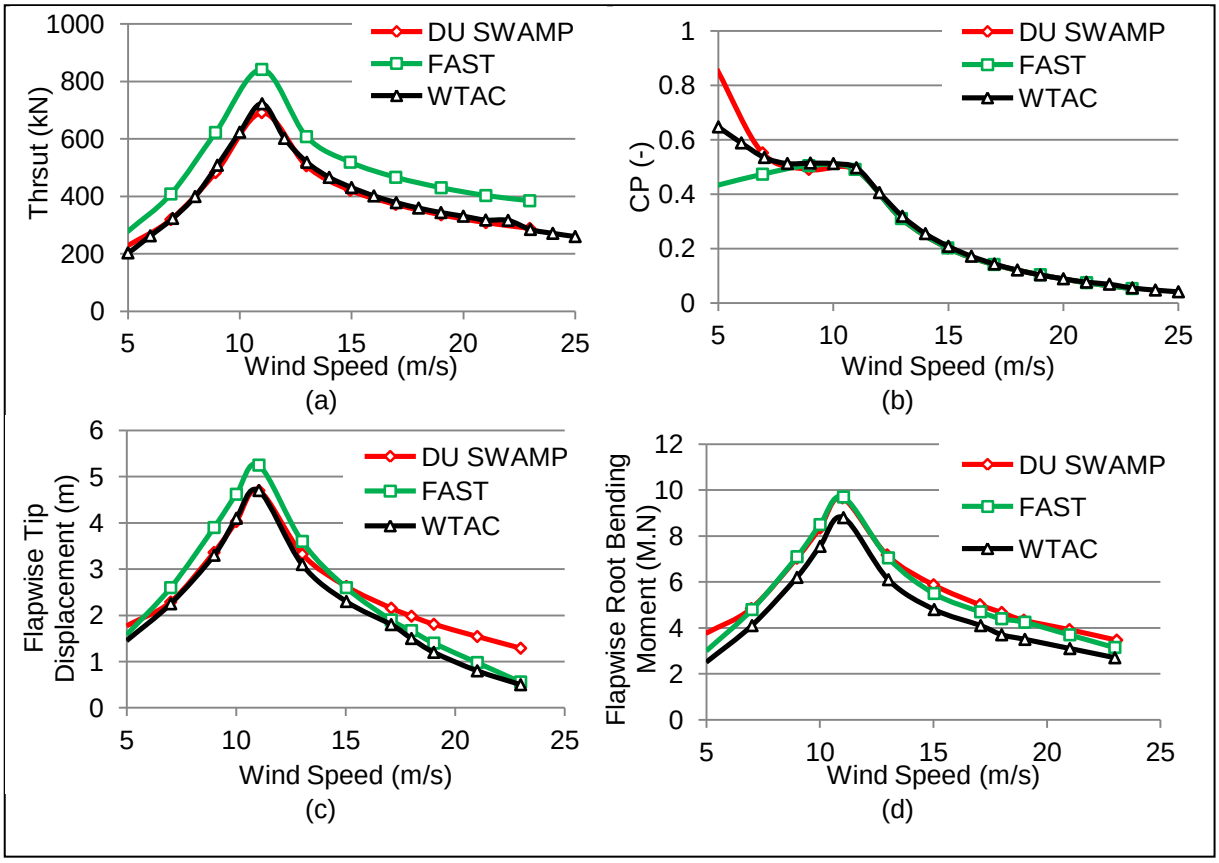

Figure 10 - Steady state results: (a) Thrust, (b) Power coefficient, (c) Flapwise tip deflection and (d) Flapwise bending moment at the root of the blade.

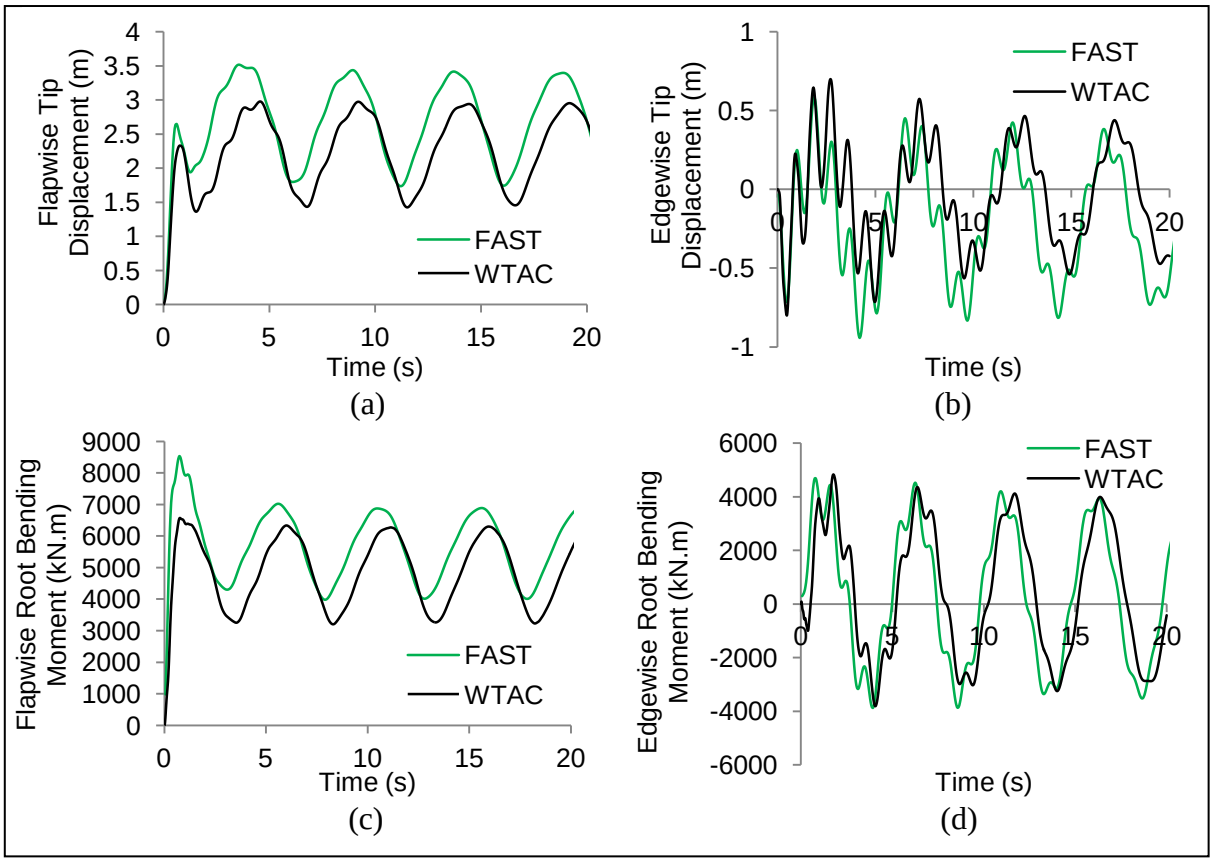

Figure 11 - (a) Flapwise tip displacement, (b) Edgewise tip displacement, (c) Flapwise bending moment and (d) Edgewise bending moment at root of the blade at a mean wind speed of 15m/s.

6 Performance of Controllers in Load Alleviation

For all controllers, it is assumed that the blade is equipped with a string of microtabs covering $S_{MT} = 12m$ (about 20%) of the total span of the NREL-5MW wind turbine blades, extending from radial location 45.7 m to 57.7 m (see Figure 12). The string of microtabs is divided into n segments, each segment with a length of ΔS_{MT} . Microtabs located on the same segment actuate simultaneously acting as a single unit, while each segment of microtabs operates independently. Without loss of accuracy, microtabs segments can be of the same length of the blade segments defined for BEMT analysis. Results presented in the rest of this paper are obtained by simulations of fixed mean wind speeds over 180 seconds with a time step of 0.01 seconds. In simulation, it is assumed that Pitot tubes and strain gages are used to postulate flow kinematics and the blade bending moment. It is assumed that one strain gage sensor per blade, located at mid span, is used. Postulation of the local flow kinematics in front of each microtab using Pitot tubes is detailed in Section 6.1. Although the wind turbine investigated in this study is equipped with a conventional pitch control system the dynamic pitching is not considered in simulation. Since pitch control system and microtabs act on two different frequency bandwidths, it is assumed that the two control systems do not have any significant interactions.

6.1 Simulating Measurement System - Local Flow Kinematic Prediction Using Pitot Tubes

Two parameters that describe the dynamic and steady behaviour of microtabs are the local relative velocity and the angle of attack. These parameters can be approximated via measured quantities by Pitot tubes, namely, the inflow angle and the local relative velocity as reported by Castaignet et al. [26, 27]. Since, in practice, it is not viable to have a Pitot tube in front of each microtab [26, 27], it is assumed that only two Pitot tubes per blade are used and the flow kinematics at other microtab locations are interpolated based on the reading of these two.

Flow kinematics at the outer parts of blades, where the microtabs are located, is mainly dictated by the magnitude of the tangential velocity rather than the axial (wind) velocity. Since tangential velocity is a linear function of radial location, using only two Pitot tube and interpolation of the flow kinematics for other points seems a reasonable arrangement. This section investigates the accuracy of postulation of flow kinematics over a long span by using only two measurement points. In this study it is assumed that the Pitot tubes are located close to the two ends of the microtab string at radial locations 47.7m and 55.7m (see Figure 12). This makes the middle segment, centred at radial location 51.7 m, the worst segment in terms of expected error in flow kinematic prediction.

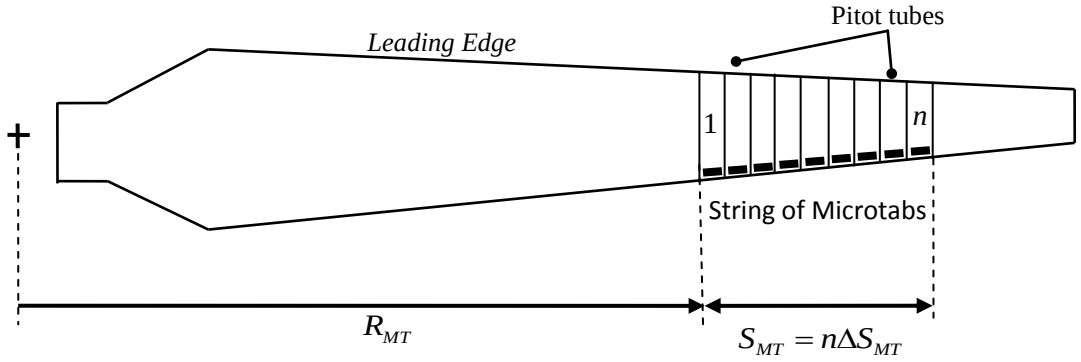

Figure 12 - Microtabs and Pitot tube Location

Using TurbSim a 180-second unsteady flow field with time step of 0.01 seconds is produced. For each time step, the angle of attack and the relative velocity distributions at radial location 51.7 m are predicted based on the values at two locations 47.7m and 55.7m (representing the two measurement points by Pitot tubes). The predicted results are then compared with the actual data produced by TurbSim and used to calculate the error of prediction. Figure 13 shows the probability density function of the error in the predicted angle of attack for the mean wind speeds of 5 and 15m/s. The fitted normal distributions to the probability density functions (also shown on Figure 13) show that for both cases μ, the error expectation, is very close to zero and σ, the standard deviation, is also very small. Referring to Figure 2, one can see that changes in angle of attack within the range of errors shown in Figure 13 have small impact on the aerodynamic coefficients.

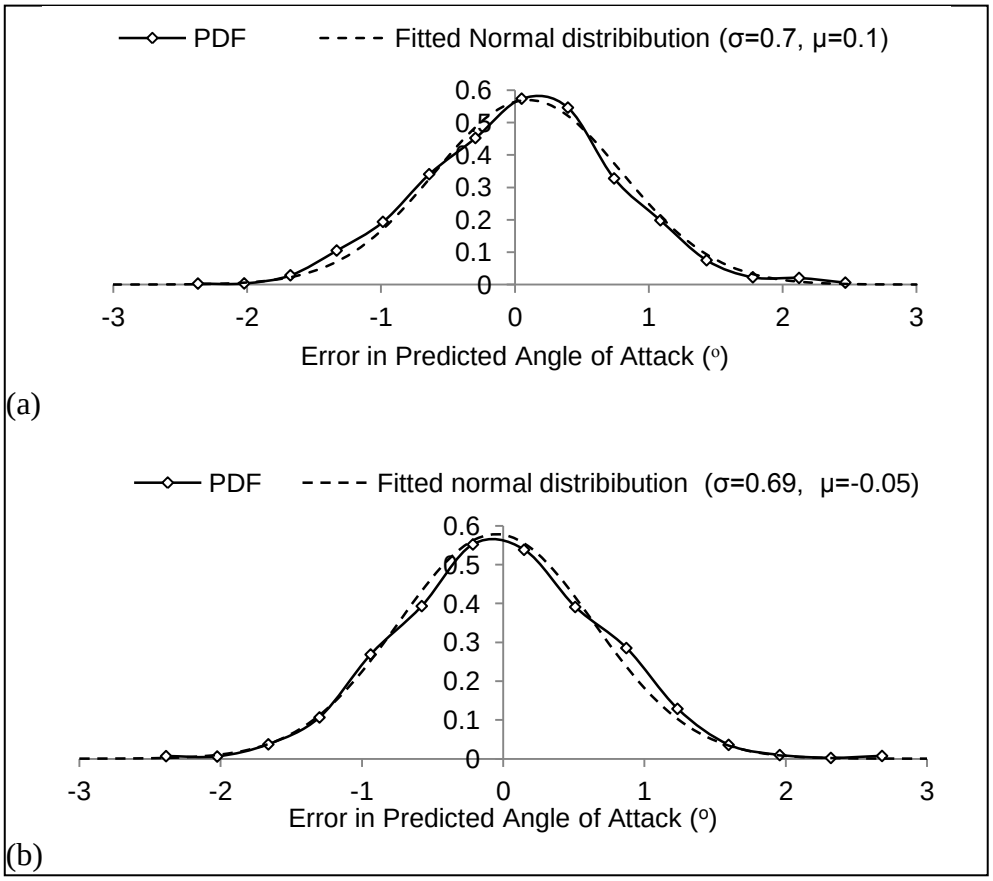

Figure 13 - Error of estimation of the angle of attack at radial location 51.7m based on Pitot measurements at radial locations 47.7m and 55.7m for mean wind speed of (a) 5m/s and (b) 15m/s.

6.2 Load Alleviation Results in Frequency Domain

The four controllers are designed to alleviate loads higher or equal to the 1*P* frequency (1*P*+), approximately equivalent to 0.2Hz for a corresponding rotor speed of $\Omega = 12.1 rpm$ at rated wind speed. A 180-second simulation of the 5MW wind turbine utilising the four controllers operating at a 10 m/s mean wind speed wind field is carried out. Representing the controlled bending moment at the root of the blade by two components, the mean value $\overline{M}_c$ and the variable part $\hat{M}_c$ ($M_c = \overline{M}_c + \hat{M}_c$), Figure 14 shows the frequency spectrum of the variable part of the controlled bending moment with particular zoom in the 1*P*, 2*P*, 3*P* frequencies (0.1923, 0.3846 and 0.5769 respectively), as well as the first flapwise natural frequency 1*N* (0.73Hz).

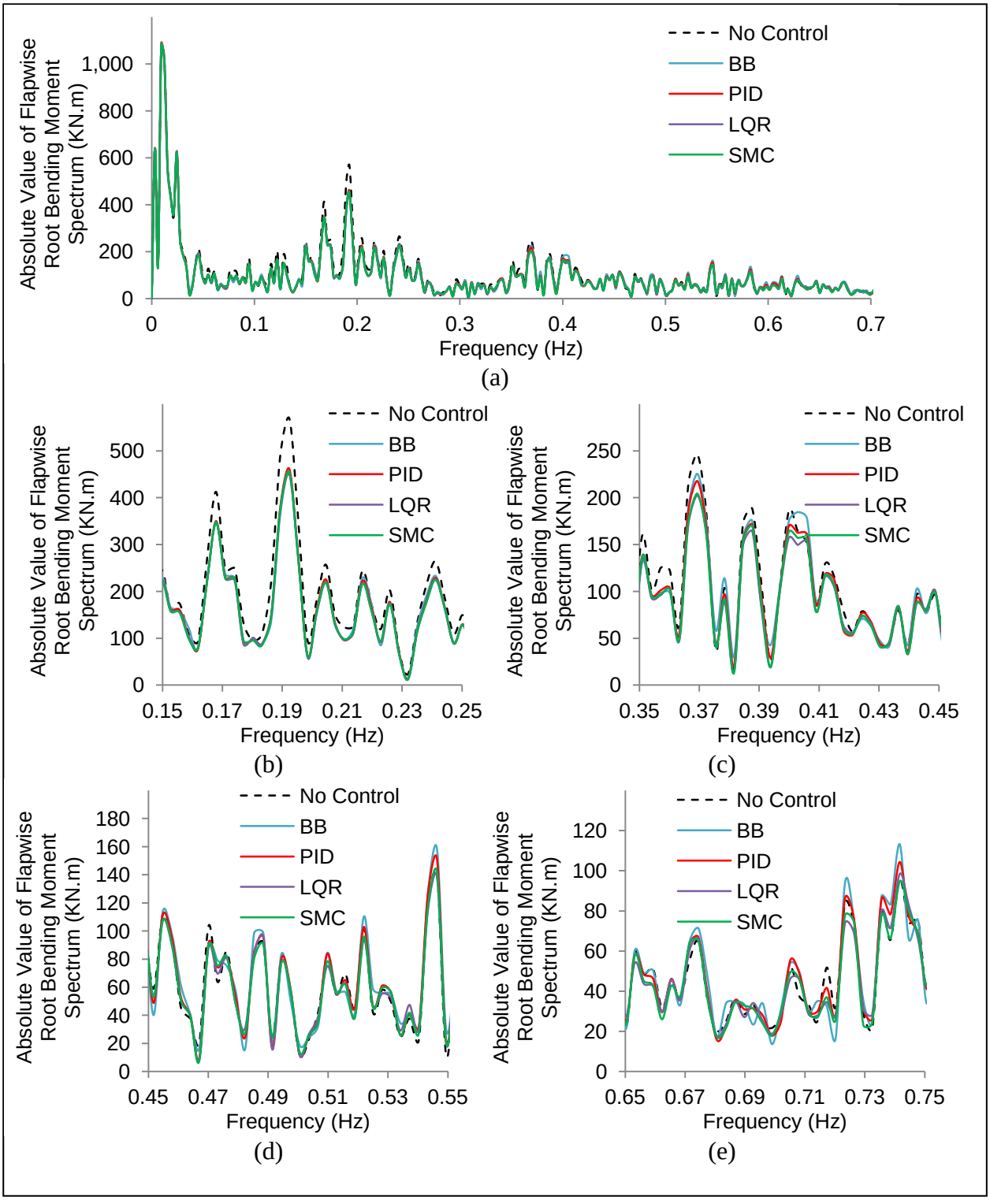

Figure 14 - (a) Load alleviation results at a mean wind speed of 10m/s; zoom in (b) 1*P*, (c) 2*P*, (d) 3*P*, (e) 1*N*.

A more quantitative assessment of the performance of different controllers can be carried out by averaging the load reduction in separate intervals centred at 1*P*, 2*P*, 3*P* and 1*N* by employing Equation 41.

$$LA = 100\left(\frac{\sum_{nP-\mu}^{nP+\mu}\left(f_{noc}(\omega) - f_c(\omega)\right)}{\sum_{nP-\mu}^{nP+\mu} f_{noc}(\omega)}\right) \tag{41}$$

in which, $f_{noc}(\omega)$ and $f_c(\omega)$ respectively denotes the load frequency spectrum for the uncontrolled and controlled case and $[nP-\mu, nP+\mu]$ is the interval over which the results are averaged for the first, second and third rotational frequencies ($n = 1,2$ and 3) as well as the first natural frequency. Table 4 shows the quantitative load alleviation calculated using Equation 41 with a 20% frequency range $(\mu = 0.2nP)$ for the simulation results shown in Figure 14.

Table 4 - Load alleviation for a mean wind speed of 10m/s for $\mu = 0.2nP$ (targeted frequency 1*P*+)

	BB	PID	LQR	SMC
1*P*	-15.87%	-15.39%	-17.05%	-16.69%
2*P*	-4.69%	-8.28%	-13.72%	-12.19%
3*P*	6.97%	1.77%	-5.45%	-5.27%
1*N*	3.49%	2.86%	-1.63%	-2.82%

With reference to Figure 14 and Table 4 one can observe that all controllers, irrespective of the actuation mechanism (discontinuous and continuous) and type (BB, SMC, LQR and PID) have very similar performance in easing 1*P* loads. This can be explained as follows: 1*P* loads are mainly caused by the variations of the aerodynamic loads due to wind shear. For this frequency, the target load to be generated by string of microtabs, ΔM_{target}, is greater than the microtab reachable space (achievable moment by the string of microtabs) and consequently all microtabs deploy to maximum height and saturation as shown in Figure 15.a, for two controllers BB (discontinuous) and PID (continuous). In other words, the deployment height time history is dominated by the effect of low frequency loads (1*P*-2*P*) as shown in Figure 15.b. This figure shows 1*P* and 1*P*-2*P* loads after filtering all other frequencies.

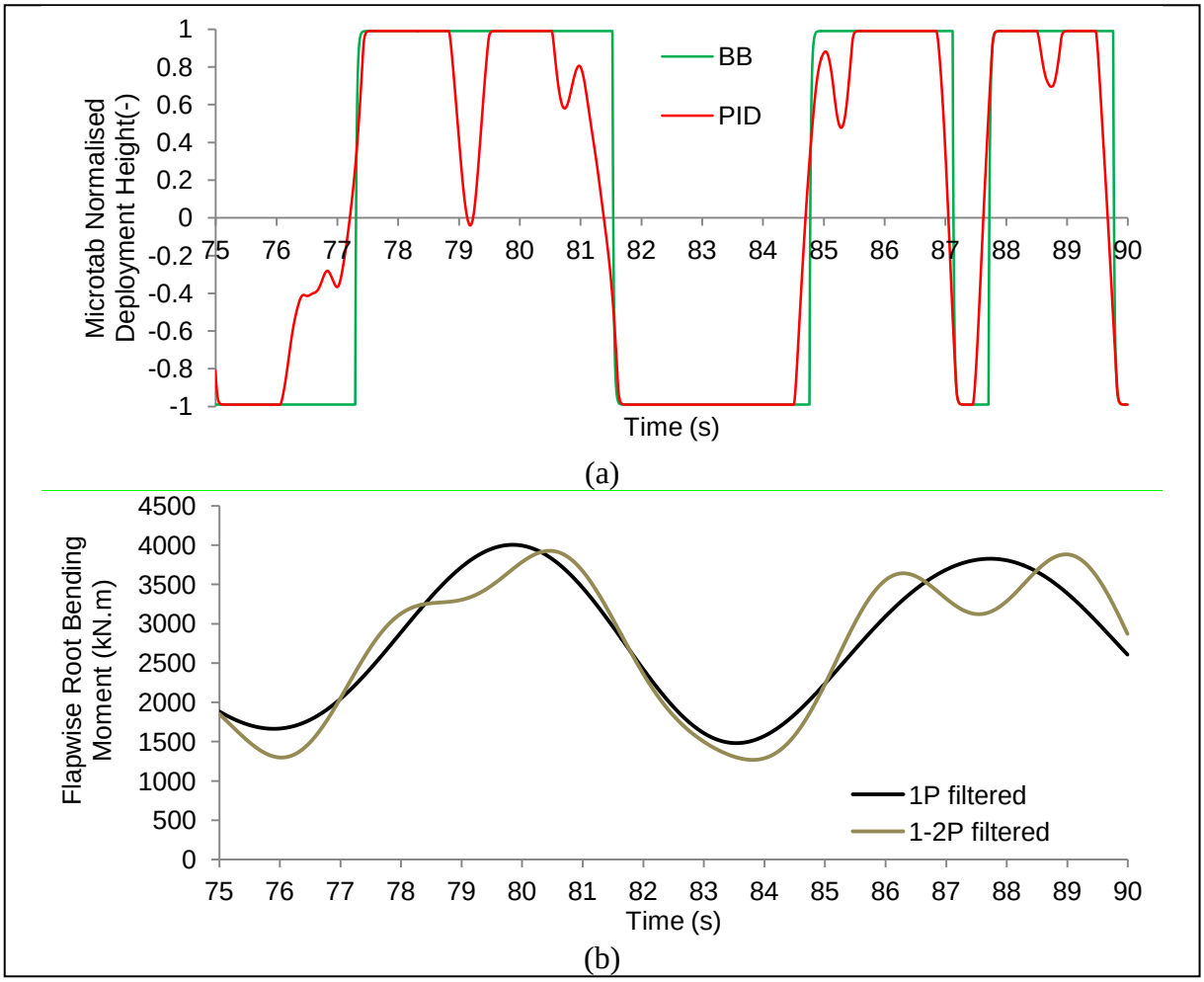

Figure 15 - (a) Microtab normalised deployment height and (b) root bending moment alleviation employing BB and PID controllers for a 15 seconds time window from a 180-second simulation for a mean wind speed of 5m/s.

Results presented in Table 4 also show that the effectiveness of all controllers in load alleviation reduces with load frequency. In fact, BB and PID controllers amplify loads with higher frequencies. A similar observation of this phenomena for trailing edge flaps has been reported in the work of Castaignet *et al.*[26] where it is explained as plant-model mismatch. However, this behaviour is due to the fact that these controllers aim at alleviating the main frequency (1*P*) without taking into account its effect on the higher frequency bandwidths. On the other hand, in the model-based controller LQR the control law does not allow the controller to increase 1*N* frequencies in order to decrease 1*P*. In case of the model-based controller SMC, the designed sliding surface aims at a reduction of all the frequencies rather than just low frequencies. Although the LQR and SMC controllers assume two different microtab deployment mechanisms (continuous and discontinuous), their load alleviation performances are comparable.

The effect of different controllers on the 1*N* loads at different wind speeds are also calculated and presented in Table 5.

Table 5 - Effect of load alleviation on first natural frequency (1*N*)

Mean wind speed (m/s)	BB	PID	LQR	SMC
5	33.84%	1.44%	-8.79%	-7.51%
10	3.49%	2.86%	-1.63%	-2.82%
15	16.23%	10.30%	-2.19%	-5.12%
22	33.34%	14.31%	-24.33%	-27.64%

From this table it can be seen that while the effect of BB and PID in amplification of high frequency loads is either unpredictable or increasing with wind speed, LQR and SMC become more effective at load alleviation at higher wind speeds due to their robustness. This can be seen as the chief advantage of LQR and SMC compared to BB and PID.

6.3 Performance in terms of actuator lifespan durability

Microtabs actuators are required to meet some design constraint in order to be considered as a potential solution for load alleviation. Microtab actuator must have a short time response to counteract high frequency aerodynamic loadings. On the other hand, while subject to high frequency deployment, microtabs must maintain their reliability over the long lifespan of wind turbine. Figure 16 shows the behaviour of the BB, SMC, PID and LQR controllers in microtabs actuation in time domain. As one can observe from this time window, the SMC clearly features the most violent microtab actuations whereas the BB controller bears the less effort on microtabs actuator.

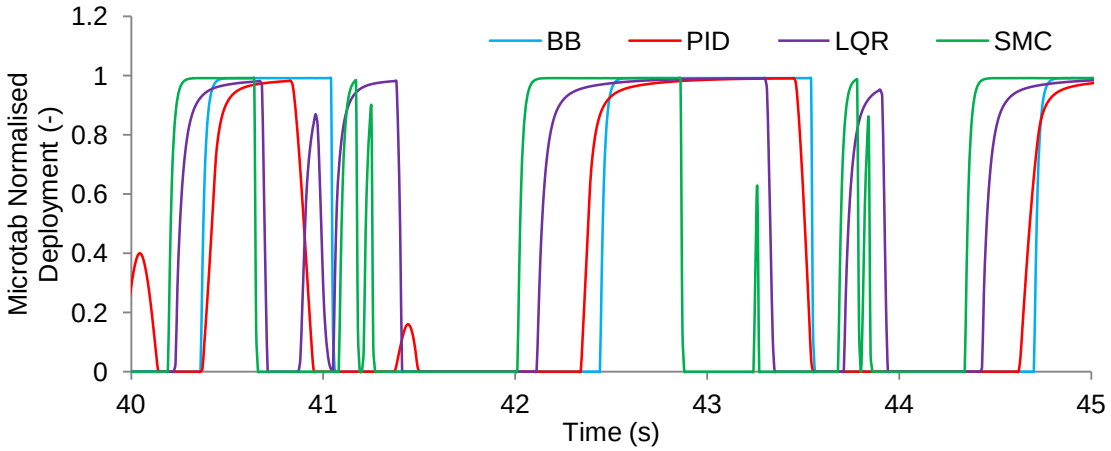

Figure 16 - Comparison of microtab actuation between the four controllers for a mean wind speed of 10m/s.

To evaluate the wear of actuators using four controllers, the number of actuations is counted for each scenario. The number of actuations here is defined as the number of changes in the sign of deployment speed. The average numbers of actuations per blade, for the respective mean wind speed of 5, 10, 15 and 22m/s, over 180 seconds simulations for the four controllers are given in Table 6.

Table 6 - Average Numbers of actuation per blades per microtab section over 180 seconds

Mean Wind Speed (m/s)	BB	PID	LQR	SMC
5	109	264	646	987
10	98	259	340	1137
15	143	237	318	829
22	202	261	649	979

According to this table evidently the lowest wear of actuators (number of actuations) corresponds to BB controllers. SMC, on the other hand due to chattering phenomenon exhibits the highest number of actuations and wear. A more quantitative comparison between the wear of actuators used by different controllers can be carried out by defining parameter life index (LI) as in Equation 42.

$$LI = \sum_{v=v_0}^{v_f} \left[\left(\int_{v-0.5\Delta v}^{v+0.5\Delta v} pdf_v dv \right) \frac{1}{[N_A]_v} \right] \quad (42)$$

In this equation pdf_v is the probability density function for a given site and N_A denotes the total number of actuations of all microtabs over all blades for one constant mean wind speed. Parameters v, v_0, v_f and Δv stand for the mean wind speed, initial wind speed, final wind speed and the wind speed increment respectively. Initial mean wind speed v_0 is equal to the cut-in speed of the wind turbine. On the other hand, v_f is the wind speed at which the capacity of microtabs to affect loads decreases toward zero (stall, post-stall or shut-down wind speed). The life index of the four controllers are calculated using Equation 42. Table 7 shows the normalised results with respect to the life index of BB controller.

Table 7 - Normalised Life index for a PDF of 3 different average mean wind speeds

Site average wind speed (m/s)	BB	PID	LQR	SMC
5.7	1.00	0.40	0.17	0.10
7	1.00	0.41	0.20	0.12
9	1.00	0.44	0.14	0.11

This table shows that the number of actuations when using SMC, as the most effective controller in load alleviation, can be as high as 10 times of the number of actuations when using BB. On the hand, the number of actuations when using LQR is only about 7 times of the number of actuations for BB controllers. Taking into account that the performance of LQR in load alleviation is comparable with the performance of SMC, LQR is probably the best type of controller for microtab actuators.

7 Summary and Concluding Remarks

The effect of controller type on the performance of microtabs in load alleviation and the life of actuators was investigated. Four types of controllers, namely, BB, PID, LQR and SMC, were synthesised for load alleviation. A software tool, WTAC, for simulation and analysis of wind turbines equipped with microtabs actuated with synthesised controllers was developed. WTAC employs an unsteady BEMT aerodynamic load predictor incorporating the microtab aerodynamic model, a reduced order aeroelastic model, and a controller simulator for aeroelastic and control analysis of wind turbines equipped with active load controls. It was shown, while capable of simulating active control systems, WTAC performance in aerodynamic and aeroelastic analysis of wind turbine blades is comparable with well known tools FAST and DU-SWAMP.

The microtab dynamic response model recently developed by Macquart et al [13] was used for simulating the microtab transient aerodynamic response as well as synthesising more realistic controllers to investigate the full potentials of microtabs.

Using WTAC to carry out frequency domain analyses it was shown that:

- Microtab, as an active control surface, can be effective in alleviating loads with a wide range of frequencies (1*P* to 1*N*).
- The controller type used to actuate microtabs plays a major role in the effectiveness of microtabs in load alleviation.
- For the studied 5MW wind turbine all controllers show more or less the same performance at rejecting the low frequency loads. This is due to saturation of microtabs when dealing

with demand loads larger than their reachable spaces. It is expected to observe different behaviour for smaller wind turbines or when using longer strings of microtabs.

- Effectiveness of all types of controllers in alleviating loads reduces with the frequency of load. While controllers LQR and SMC are still capable of rejecting loads with higher frequencies, simple controllers BB and PID amplify high frequency loads including the first natural frequency of the blade. The effectiveness of BB and PID controllers reduces with wind speed but on the other hand SMC and LQR perform better at higher wind speeds. This is due to using a high-pass filter as reference to the controllers, leading the control system to provide more control effort for alleviating lower frequency bandwidths.
- Discontinuous and continuous actuation methods can produce similar load relief if suitable controllers (SMC and LQR) are used.
- LQR causes less wear while having a load alleviation performance comparable with SMC.

8 References

[1] T.J. Larsen, H.A. Madsen, K. Thomsen, Active load reduction using individual pitch, based on local blade flow measurements, Wind Energy, 2005; Vol.8: 67-80.

[2] T.G. Van Engelen, Design model and load reduction assessment for multi-rotational mode individual pitch control (higher harmonics control), Wind Energy Conference 2006.

[3] S.J. Johnson, J.P. Baker, C.P. van Dam, D. Berg, An overview of active load control techniques for wind turbines with an emphasis on microtabs, Wind Energy, 2010. 13(2-3): p. 239-253.

[4] P. Bæk, M.Gaunaa, N.N. Sørensen, P. Fuglsang, Comparative Study of Distributed Active Load Control Concepts for Wind Turbine Blades, Science of Making Torque from Wind, 2010: p. 611-617.

[5] D.T. Yen, C.P. van Dam, F. Bräeuchle, R.L. Smith, S.D. Collins, Active Load Control and Lift Enhancement Using MEM Translational Tabs, Fluids 2000, AIAA Paper 2000-2422, 2000; [Denver, CO].

[6] R. Chow, C.P. van Dam, Computational Investigations of Deploying Load Control Microtabs on a Wind Turbine Airfoil, 45thAIAA-2007-1018, 2007; [Reno, NV].

[7] J.P Baker, K.J. Standish, C.P. van Dam, Two-dimensional wind tunnel and computational investigation of a microtab modified airfoil, Journal of Aircraft, 2007. Vol.44: p. 563-572.

[8] C.P. van Dam, D. Yen-Nakafuji, C. Bauer, D. Chao, K. Standish, Computational Design and Analysis of a Microtab Based Aerodynamic Loads Control System for Lifting Surfaces, SPIE International Society for Optical Engineers, 2002; [San Jose, California].

[9] P. Baek, M. Gaunaa, Modelling the Temporal Response of a Microtab in an Aeroelastic Model of a Wind Turbine, 49thAIAA, 2011. DOI: 10.2514/6.2011-348

[10] D.G. Wilson, D.E. Berg, M.F. Barone, J.C. Berg, B.R. Resor, D.W. Lobitz, Active aerodynamic blade control design for load reduction on large wind turbines, European Wind Energy Conference 2009; [Marseille, France].

[11] D.G. Wilson, D.E. Berg, D.W. Lobitz, J.R. Zayas, Optimized Active Aerodynamic Blade Control for Load Alleviation on Large Wind Turbines, AWEA Windpower, 2008; Conference & Exhibition, [Houston, Texas].

[12] J.R. Zayas, C.P. van Dam, R. Chow, J.P. Baker, Mayda EA. Active aerodynamic load control for wind turbine blades in European Wind Energy Conference 2006 [Athens, Greece].

[13] T. Macquart, A. Maheri, K. Busawon, Microtab Dynamic Modelling for Wind Turbine Blade Load Rejection, Renewable Energy, 2014; 64: 144-152.

[14] M. Frederick, E.C. Kerrigan, J.M.R. Graham, Gust alleviation using rapidly deployed trailing-edge flaps. Journal of Wind Engineering and Industrial Aerodynamics 98; 2010.

[15] E.A. Mayda, C.P. van Dam, D. Yen-Nakafuji, Computational investigation of finite width microtabs for aerodynamic load control. AIAA Paper 1185, 2005.

[16] J. Jonkman, S. Butterfield, W. Musial, G.Scott, Definition of a 5-MW reference wind turbine for offshore system development; 2009, National Renewable Energy Laboratory Colorado.
[17] S.S. Collis, R.D. Joslin, A. Seifert, V. Theofilis, Issues in active flow control: theory, control, simulation, and experiment, Progress in Aerospace Sciences, 2004: p. 237-289.
[18] A. Maheri, S. Noroozi, C. Toomer, J. Vinney, WTAB, a Computer Program for Predicting the Performance of Horizontal Axis Wind Turbines with Adaptive Blades, Renewable Energy, 2006; 31(11): 1673-1685.
[19] J.W. Larsen, S.R.K. Nielsen, S. Krenk, Dynamic stall model for wind turbine airfoils, Journal of Fluids and Structures, 2007; 23(7): 959-982.
[20] J.T. Foley, T.G. Gutowski, TurbSim: Reliability-based wind turbine simulator, 2008 IEEE International Symposium on Electronics and the Environment, 2008; 315-319.
[21] J.B. Gunda, A.P. Singh, P.S. Chhabra and R.Ganguli, Free vibration analysis of rotating tapered blades using Fourier-p superelement. Structural Engineering and Mechanics, 2007. **27**(2): p. 243-257.
[22] G. Wang, N.M. Wereley, Free vibration analysis of rotating blades with uniform tapers. AIAA journal, 2004. **42**(12): p. 2429-2437.
[23] J. Jonkman, M. Buhl, FAST user's guide. Golden, CO: National Renewable Energy Laboratory (2005).
[24] B. Resor, D. Wilson, D. Berg, J. Berg, Impact of higher fidelity models on simulation of active aerodynamic load control for fatigue damage reduction. Proceedings of the 48th AIAA/ASME, 2010.
[25] T. Macquart, A. Maheri, K. Busawon, Improvement of the Accuracy of the Blade Element Momentum Theory Method in Wind Turbine Aerodynamics Analysis, International Symposium On Environment Friendly Energies And Applications 2012.
[26] D. Castaignet, N.K. Poulsen, T. Buhl, J.J. Wedel-Heinen, Model Predictive Control of Trailing Edge Flaps on a Wind Turbine blade, American Control Conference, 2011. p. 4398-4403.
[27] D. Castaignet, I. Couchman, N.K. Poulsen, T. Buhl, J.J. Wedel-Heinen, Frequency-Weighted Model Predictive Control of Trailing Edge Flaps on a Wind Turbine Blade, IEEE Transaction on control system technology, vol.21, No 4, 2013

List of Figures

List of Tables